

## Corrosion Behavior of X80 Pipeline Steel under Thin Electrolyte Layer of Acidic Soil Simulated Solution

Shuaixing Wang<sup>1,2,\*</sup>, Daoxin Liu<sup>1</sup>, Nan Du<sup>2</sup>, Qing Zhao<sup>2</sup>, Jinhua Xiao<sup>2</sup>

<sup>1</sup> Institute of Corrosion and Protection, Northwestern Polytechnical University, Xi'an 710072, China

<sup>2</sup> School of Material Science and Technology, Nanchang Hangkong University, Nanchang 330063, China

\*E-mail: [wsxxpg@126.com](mailto:wsxxpg@126.com)

Received: 13 January 2016 / Accepted: 1 February 2016 / Published: 1 March 2016

---

Corrosion behavior of X80 steel under thin electrolyte layer (TEL) of acidic soil simulated solution were studied by utilizing polarization curves, EIS, SEM and XRD. In the bulk solution, cathodic electrochemical reaction governed the corrosion process of X80 steel, and the corrosion rate was higher. Under TEL, the corrosion of X80 steel was greatly affected by TEL thickness. Under TEL of 300  $\mu\text{m}$ , the corrosion was still related to the cathodic electrochemical process. Under TEL of 145  $\mu\text{m}$ , oxygen diffusion dominated the corrosion process, and the corrosion rate fluctuated with immersion time. However, the corrosion of X80 steel was jointly affected by the diffusion processes of oxygen and corrosion products under TEL of 70  $\mu\text{m}$ . In this system, the corrosion rate increased continuously. After 96 h exposure, the corrosion extent of steel with TEL thickness was in the sequence of 70  $\mu\text{m}$  > 300  $\mu\text{m}$  > 145  $\mu\text{m}$ . Complete corrosion product layer was easier to form in the thinner TEL.

---

**Keywords:** X80 steel; Acidic soil; Corrosion; Thin electrolyte layer (TEL); EIS

### 1. INTRODUCTION

X80 steel is widely used for building crude oil and gas transmission pipelines as its satisfactory combination of strength, toughness and weld ability [1, 2]. As buried pipelines, the organic coatings have been recognized as the most effective method to protect pipelines from external corrosion in soil [3, 4]. Generally, the complete coating shields the steel pipe from the corrosive environment. However, the corrosive species and oxygen can penetrate through coating to reach the coating/steel interface when the faults exist in the protective coating. As a result, stress corrosion cracking (SCC) [5-7], crevice corrosion [8-10] and other kinds of localized corrosion [11-13] may be observed under disbonded coatings, which present a great uncertainty to pipeline companies in terms of risk management.

In southeastern and south china, red clay soils are the dominant soils. Besides, the acid rain with pH of 2.3 ~5.9 often occurs in these regions [14]. It has been found that acidic red soils are extremely aggressive towards carbon steel [15], and acid rain can result in the failure of protective coating [16,17]. When red clay soil was leached by acid rain, the leaching solution will be formed through the ions exchange. The leaching solution can reach the coating/steel interface through the cracks of disbonded coating and form the trapped electrolyte. The trapped electrolyte between coating and the steel is found to be very thin [5, 10]. Electrochemical corrosion of steel under thin electrolyte layer (TEL) of leaching solution is distinctly different from that in the red soil, and also has great difference with that in the TEL of acid rain. For example, the small ohmic potential drop and non-uniform current distribution under TEL are expected to affect significantly the electrochemical mechanism for corrosion of steel [18]. It has been acknowledged that the corrosion of buried pipeline usually began and developed from the disbonded coating [5-11]. The thickness and chemical composition of TEL between the disbonded coating and steel have significant effect on the corrosion behavior of steel. Therefore, it is necessary to study the electrochemical corrosion mechanism of X80 steel under TEL of acidic soil leaching solution.

Currently, SCC and crevice corrosion of pipeline steel under disbonded coating in soil environment has been investigated by various electrochemical measurement techniques and computational simulation[5, 6, 8-10, 19-24]. Yan [9, 10] demonstrated that the local potential of X70 steel in a crevice simulating disbonded coating is independent on cathodic protection (CP) potential applied at the opening. Fu [19] found that X65 steel has a more negative Kelvin potential on the area of disbonded coating than that on “intact” area. The corrosion behavior of X65 steel under disbonded coating strongly depends on the oxygen partial pressure and local geometry. In addition, some scholars investigated the effect of acid rain on the corrosion of steel in acid soils [16, 25-26]. Wu [16] found that the extent of corrosion is highly dependent on the pH of acid rain, and that the soil itself is further acidified with the application of acid rain. However, to date, there has been limited work investigating the corrosion behavior of pipeline steel under thin electrolyte layer of leaching solution form soil. Only the electrochemical corrosion behavior of X70 steel in a thin layer of near-neutral pH and high pH soil solutions were studied by Fu [27] and Yan [28].

In this work, the corrosion behavior of X80 steel under a thin electrolyte layer of acidic soil simulated solution was characterized by polarization curves and electrochemical impedance spectroscopy (EIS). The influence of TEL thicknesses on the corrosion mechanism of X80 steel was analyzed. It was anticipated that this research provides an essential insight into corrosion of X80 steel under disbonded coating in acidic soil environment.

## 2. EXPERIMENTAL

### 2.1 Materials and solution

The test material is API-X80 pipeline steel with the chemical composition showed in Table 1. The X80 steel with the area of 10 mm× 10 mm is embedded in epoxy resin to act as working electrode.

These specimens are successively abraded with SiC emery papers, rinsed with distilled water for 2 min, ultrasonicated in alcohol for 10 min, and dried in an air flow.

Yingtian ( $28^{\circ}15' N$ ,  $116^{\circ}55' E$ ) is regarded as a representative region of acidic red clay soil in South China. The simulating solution is prepared according to the analysis data of Yingtian soil. The main chemical compositions is given in Table 2. Besides, the solution pH is adjusted to  $4.5 \pm 0.2$  by adding sulfuric acid according to the acidity and the main active ion ( $SO_4^{2-}$ ) of acid rain in this region.

**Table 1.** Chemical composition (wt.%) of X80 steel

C	Si	Mn	P	Mo	Nb	Ti	Cr	Ni	Cu	Al	Fe
0.036	0.197	1.771	0.012	0.184	0.110	0.019	0.223	0.278	0.220	0.021	bal.

**Table 2.** Chemical composition of acidic soil (Yingtian soil) simulated solution

Compounds	NaCl	CaCl <sub>2</sub>	MgSO <sub>4</sub> ·7H <sub>2</sub> O	Na <sub>2</sub> SO <sub>4</sub>	NaHCO <sub>3</sub>	KNO <sub>3</sub>
Content (g/L)	0.0468	0.0111	0.0197	0.0142	0.0151	0.0293

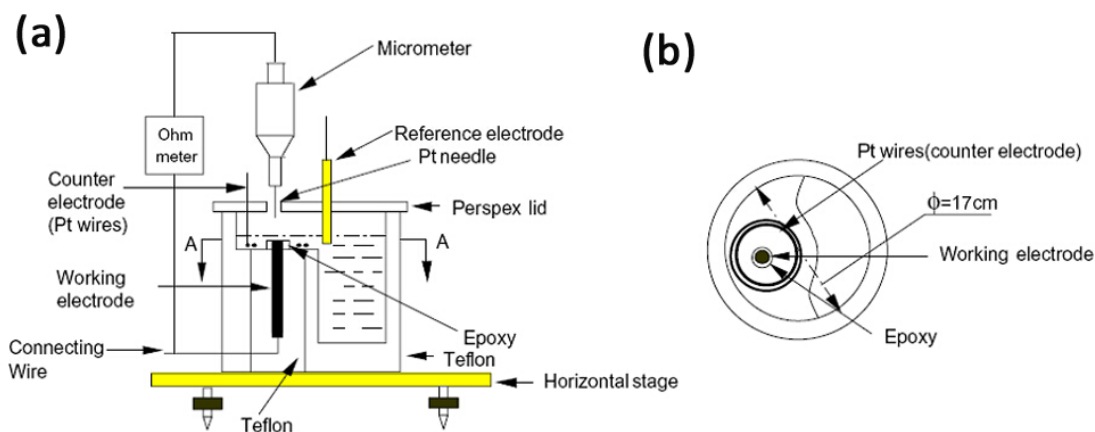
## 2.2 Determination of TEL thickness

Figure 1 is a schematic diagram of experiment arrangement for thin electrolyte layer which widely used by many scholars [29-31]. A digimatic micrometer (INSIZE 6353-25C, unit.  $\pm 2 \mu m$ ) with a fine Pt-needle is fixed at a position right above the electrode. When Pt-needle is adjusted to touch the electrode surface, there will be a sudden value on the ohmmeter. The position of the micrometer is recorded. Afterwards the micrometer is moved backward, and the electrolyte is poured into the cell to form a electrolyte film on the electrode. The ohmic meter will show a sudden ohmic value when the Pt-needle is moved to touch the electrolyte layer surface. And the position of the micrometer is recorded again. The thickness of electrolyte layer can be calculated from the two value of micrometer. This arrangement allows the measurement of TEL thickness with an accuracy of  $2 \mu m$ . Besides, to keep the constant of TEL thickness for a long time during electrochemical measurements, the cell is placed inside the desiccator.

## 2.3 Electrochemical test

Electrochemical tests are conducted by Autolab PGSTAT 302N in a three-electrode cell system. The test setup is shown in Figure 1. X80 steel mounted in epoxy resin with an exposure area of  $1.0 \text{ cm}^2$  is used as the working electrode. It is fixed firmly in the cell, leaving only the upper surface exposed. A Pt wire circling the working electrode is used as the counter electrode and positioned lower than the working electrode surface. A saturated calomel electrode (SCE) is used as the reference electrode.

Polarization curves are measured potentiodynamically from  $-2.0$  V (vs. SCE) to  $1.25$  V (vs. SCE) at a scan rate of  $1$  mV/s. EIS spectra for X80 steel during  $96$  h exposure in the electrolyte layers are acquired at open-circuit potential over the frequency range of  $10^5 \sim 10^{-2}$  Hz using an AC signal amplitude of  $10$  mV. The equivalent circuits are fitted using the Zsimpwin software. All tests are performed at  $25 \pm 2$  °C. All tests are repeated by three duplicate specimens to confirm reproducibility of the results, and the average of the three measurements is reported in this work.



**Figure 1.** Schematic diagram of experiment arrangement for thin electrolyte layer [29-31].

## 2.4 Surface characterization

After  $96$  h exposure, the morphology of corroded X80 steel is observed by KH-7700 three-dimensional microscope and scanning electron microscopy (SEM, QUANTA-200). Besides, the phase composition of corrosion product is investigated by X-ray diffraction (XRD, Bruker D8-Advance) with a scan range from  $20^\circ$  to  $80^\circ$  (in  $2\theta$ ).

## 3. RESULTS AND DISCUSSION

### 3.1 Polarization curves

Figure 2 presents the polarization curves of X80 steel in acidic soil simulated solutions and TEL with various thicknesses after  $1$  h. Table 3 gives the corresponding fitting results. As shown in Figure 2 and Table 3, X80 steel had lowest corrosion potential ( $E_{corr}$ ) and biggest cathodic current density in bulk solution. For TEL with different thickness, the corrosion rates of X80 steel were closely related to the TEL thickness. When TEL thickness decreased from  $300$   $\mu\text{m}$  to  $145$   $\mu\text{m}$ , both the cathodic current density and corrosion current density ( $i_{corr}$ ) of X80 steel decreased. The cathodic current density obviously increased and the  $E_{corr}$  increased if TEL thickness decreased from  $145$   $\mu\text{m}$  to  $100$   $\mu\text{m}$ . However, the cathodic current density slightly decreased and the corrosion rate of X80 steel slowed when TEL thickness was down to  $70$   $\mu\text{m}$ . Besides, X80 steel was passivated with a small passive potential range under TEL of  $70$   $\mu\text{m}$ .

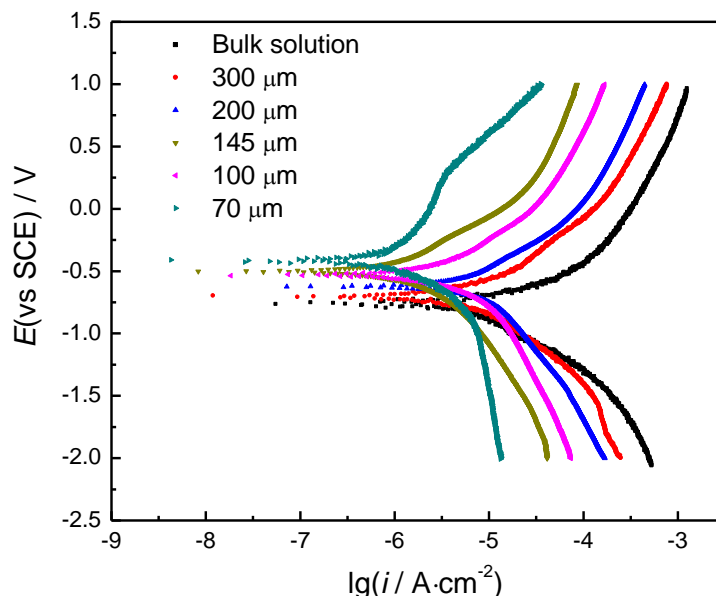


Figure 2. Polarization curves of X80 steel under TEL with various thicknesses after 1 h exposure.

Table 3. Polarization fitting results of X80 steel under TEL with various thicknesses

System	bulk solution	300μm TEL	200μm TEL	145μm TEL	100μm TEL	70μm TEL
$E_{corr}$ (V, SCE)	-0.782	-0.705	-0.628	-0.534	-0.504	-0.341
$i_{corr}$ ( $\mu A \cdot cm^{-2}$ )	1.698	0.436	0.562	0.144	0.234	0.168

### 3.2 Evans model

In order to determine the control factor of corrosion rate for X80 steel in bulk solution and TEL with various thicknesses, it was attempted to make Evans diagram by the experimental results in Figure 2 and Table 3. Generally, corrosion of steel in soils is an electrochemical process. The corrosion rate of steel is determined by the cathodic process and anodic process, according to Evans theory. It has been acknowledged [8, 32-33] that the anodic process of corrosion for X80 steel is the dissolution of Fe (Eq.1), the cathodic reaction of corrosion includes the depolarization of  $H^+$  (Eq. 2) and oxygen (Eq. 3) in the acidic soil environment.



According to Nernst equation (Eq.4, 5, 6), the equilibrium potential of the reactions can be determined.

$$E_{Fe^{2+}/Fe}^e = -0.684 + 0.0296 \lg a_{Fe^{2+}} \text{ (V, SCE)} \tag{4}$$

$$E_{H^+/H_2}^e = -0.244 - 0.0591 \text{ pH (V, SCE)} \tag{5}$$

$$E_{O_2/H_2O}^e = 0.985 - 0.0591 \text{ pH (V, SCE)} \tag{6}$$

Where, the pH and DO concentration of simulated solution were about 4.0 and 4.12 ppm, respectively. Besides, it was assumed that the metal corrodes if the concentration of metal ion in the solution was greater than  $10^{-6} \text{ mol}\cdot\text{L}^{-1}$  in potential-pH diagram. So,  $a_{Fe^{2+}}$  could be considered as  $10^{-6} \text{ mol}\cdot\text{L}^{-1}$ . The aboving calculations showed that  $E_{Fe^{2+}/Fe}^e$ ,  $E_{H^+/H_2}^e$  and  $E_{O_2/H_2O}^e$  were -0.8613 V , -0.4804 V and 0.7486 V, respectively.

It can be found that  $E_{Fe^{2+}/Fe}^e < E_{corr} < E_{H^+/H_2}^e < E_{O_2/OH^-}^e$ , which showed that oxygen-consuming corrosion initially occurred when X80 steel was immersed into acidic soil simulated solution. Hydrogen evolution corrosion began only when oxygen concentration was down to some extent. That was, the depolarization of oxygen dominated the cathodic process of corrosion of X80 steel. So Evans diagram for X80 steel under TEL with various thicknesses was obtained and showed in Figure 3. As shown in Figure 3, the corrosion of X80 steel was controlled by the cathodic process in bulk solution and thicker TEL (300 – 145  $\mu\text{m}$ ). The corrosion current density was biggest under TEL of 200  $\mu\text{m}$ . TEL thickness decreased, the anodic polarization degree increased. The corrosion of X80 steel was jointly controlled by cathodic process and anodic process under TEL of 70  $\mu\text{m}$ . In this system, the corrosion current density of X80 steel was smaller.

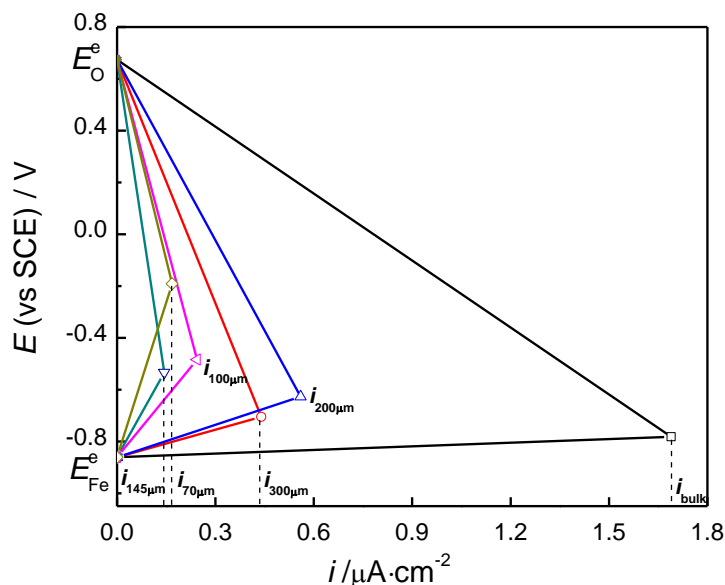


**Figure 3.** Evans diagram for X80 steel under bulk solution and TEL with various thicknesses

### 3.3 EIS behavior

Evolution of EIS plots for X80 steel during 96 h exposure in acidic soil simulated solution and TEL with various thicknesses are shown in Figure 4. In the bulk solution (Figure 4a), Nyquist plots of X80 steel displayed an incomplete loop at high frequencies and a depressed semicircle at low frequencies. The low-frequency loop indicated that the corrosion processes of steel were mainly controlled by a charge-transfer process. The high-frequency arc was attributed to the response of corrosion products [10, 12, 34-36].

Under TEL, the high-frequency arcs were always present, but the low-frequency plots were affected by TEL thickness. Under TEL of 300  $\mu\text{m}$  (Figure 3b), Nyquist plots of X80 steel were still composed of two capacitive arcs during the whole exposure, indicating that the corrosion process was still controlled by electrochemical activation reaction. Whereas, the almost 45° line, the typical characteristics of Warburg impedance, appeared in the low-frequency region of Nyquist plots for X80 steel under TEL of 145  $\mu\text{m}$  ~ 70  $\mu\text{m}$ . It indicated that the corrosion of X80 steel was changing to the diffusion control, including the diffusion process of oxygen or corrosion products [30, 35, 37]. Besides, the integrity of high-frequency arc for EIS plots obviously increased with decreasing TEL thickness, showing that complete corrosion product layer was easier to form in the thinner TEL.

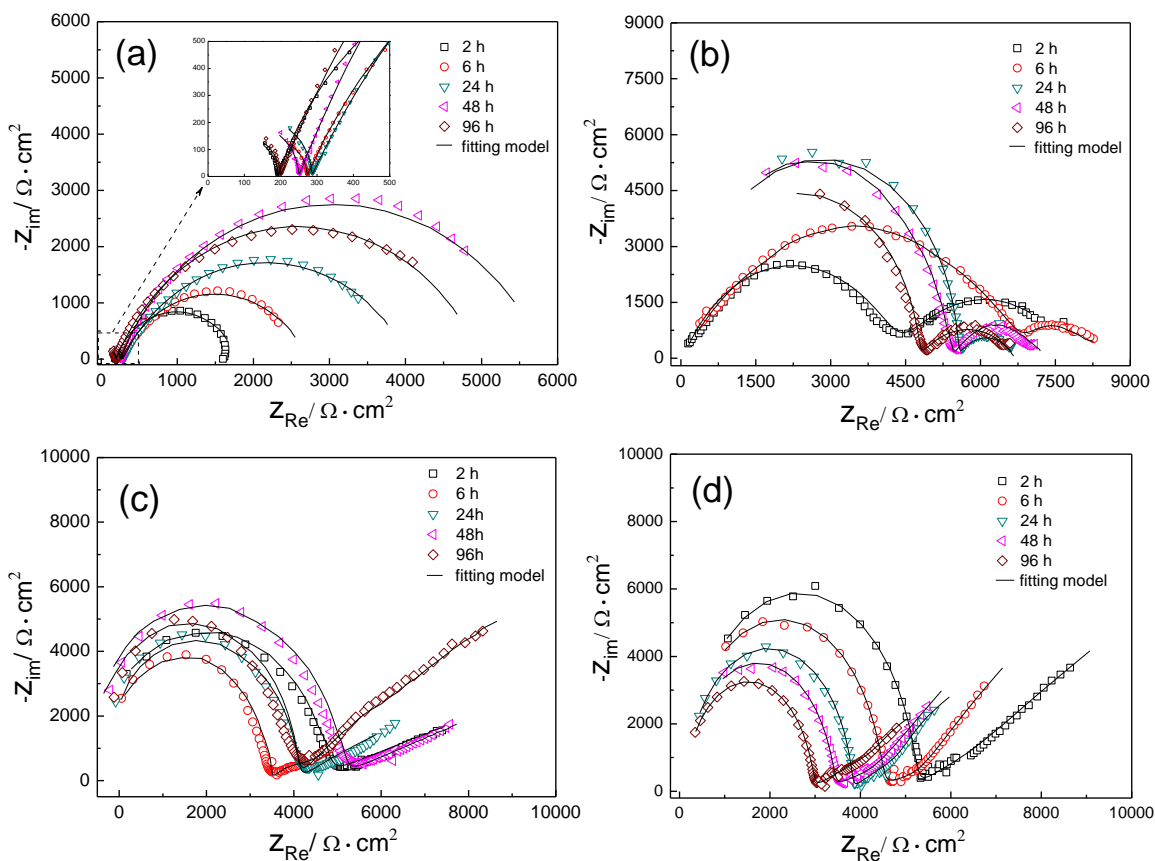


**Figure 4.** Nyquist plots of X80 steel under TEL with various thicknesses for 96h. (a) bulk solution; (b) 300  $\mu\text{m}$  TEL; (c) 145  $\mu\text{m}$  TEL; (d) 70  $\mu\text{m}$  TEL

According to the above analysis, equivalent electrical circuit in Figure 5a can be used to characterize the EIS data for X80 steel in bulk solution and TEL of 300  $\mu\text{m}$ . Where,  $R_s$  represents the electrolyte resistance. A pair of  $C_{dl}$  and  $R_{ct}$  in parallel characterizes the low frequency loop,  $R_{ct}$  is the charge transfer resistance,  $C_{dl}$  represents the double layer capacitance at the metal-solution interface.  $Q_f$  and  $R_f$  correspond to the non-ideal capacitance and resistance of corrosion product layer, respectively. In addition, there is Warburg impedance in EIS plot for X80 steel under TEL of 145  $\mu\text{m}$  ~ 70  $\mu\text{m}$ . So  $Z_w$  is used to represent the diffusion resistance of oxygen and corrosion products, as shown in Figure 5b. Where,  $Q$  is a constant phase element,  $Q = Y_0^{-1}/(j\omega)^n$ ,  $n$  is the frequency

dispersion factor and varies from 1 to 0.  $Z_w = (j\omega)^{-0.5} Y_w^{-1}$ ,  $Y_w$  is a constant, the smaller  $Y_w$  showed the bigger diffusion resistance of medium [30, 37]. As shown in Figure 4, the equivalent circuits fitted the experimental data well in most of the frequency range, indicating that the equivalent circuits of Figure 5 were suitable.

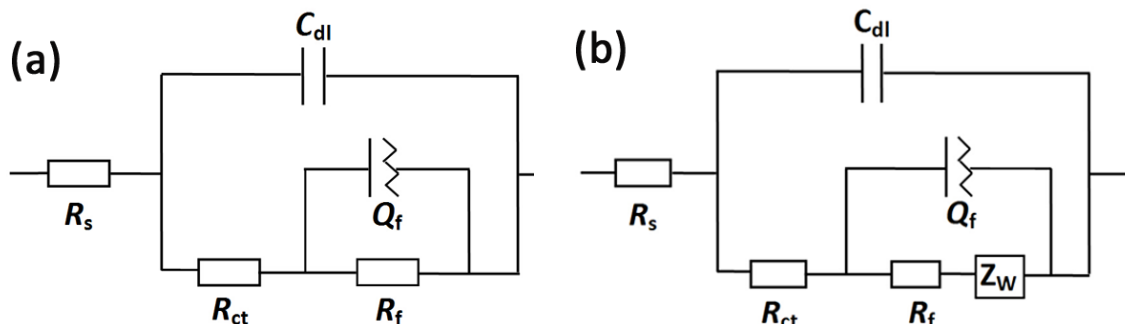


**Figure 5.** Equivalent circuits used to fit EIS for X80 steel under TEL of simulated red soil solution: (a) bulk solution and 300 μm TEL; (b) 145 μm TEL and 70 μm TEL

**Table 4.** Electrochemical parameters fitted from EIS for X80 steel under TEL with various thicknesses

System	Exposure time (h)	$R_{ct}$ ( $\Omega \cdot \text{cm}^2$ )	$C_{dl}$ ( $\mu\text{F} \cdot \text{cm}^{-2}$ )	$R_f$ ( $\Omega \cdot \text{cm}^2$ )	$Q_f$ ( $\mu\text{F} \cdot \text{cm}^{-2}$ )	$n_f$	$Y_w$ ( $\text{O}^{-1} \cdot \text{S}^{1/2} \cdot \text{cm}^{-2}$ )
Bulk solution	2	1280	64.78	562	29.33	0.2589	--
	6	1175	83.59	828	58.88	0.2805	--
	24	1864	45.9	1721	38.36	0.2713	--
	48	1322	65.0	1204	32.82	0.2532	--
	96	1661	49.58	1593	31.52	0.2242	--
300 μm TEL	2	3995	120.6	1679	31.56	0.3646	--
	6	5327	140.8	1426	43.08	0.4295	--
	24	5091	46.02	1367	10.64	0.3951	--
	48	5195	41.47	2347	13.27	0.3783	--
	96	4398	49.77	1956	13.12	0.3584	--
145 μm TEL	2	5021	58.73	1018	26.70	0.5362	0.00119
	6	3996	84.62	719	26.84	0.6348	0.00276
	24	4741	84.99	1938	42.54	0.5694	0.00345
	48	5620	74.90	2177	30.03	0.5441	0.00240
	96	5094	86.04	2675	16.24	0.4818	0.000176
70 μm TEL	2	6491	37.22	521	22.72	0.7794	0.000919
	6	4617	38.39	1136	41.03	0.7169	0.000696
	24	4250	81.77	1342	36.21	0.6963	0.000279
	48	4068	45.33	1806	22.09	0.7388	0.000290
	96	3785	107.3	2157	44.71	0.7397	0.000258

Table 4 shows the fitting component values for EIS. Generally,  $R_{ct}^{-1}$  is taken as a parameter to characterize the corrosion rate [30, 31, 37]. Figure 6 presents the evolution of  $R_{ct}^{-1}$  for X80 steel under

TEL with various thicknesses. As shown in Figure 6, the corrosion rate of X80 steel in bulk solution was significantly bigger than that of in TEL, and  $R_{ct}^{-1}$  fluctuated with immersion time. The corrosion rate of X80 steel under TEL was closely dependent on the TEL thickness. Under TEL of 300  $\mu\text{m}$ ,  $R_{ct}^{-1}$  showed a rapid decrease in the initial stage (2~6 h), and then slightly fluctuated with immersion time.  $R_{ct}^{-1}$  increased greatly at first and then showed a decrease trend with time when TEL was 145  $\mu\text{m}$ . Whereas,  $R_{ct}^{-1}$  increased continuously with the increase of immersion time under TEL of 70  $\mu\text{m}$ . After 96 h exposure, the corrosion rate of X80 steel under TEL with different thickness was ranked as 70  $\mu\text{m}$  > 300  $\mu\text{m}$  > 145  $\mu\text{m}$ .

In addition,  $R_f$  and  $n_f$  can display the features of the corrosion products. The value of  $n$  is about 0.5~1.0 for the protective corrosion product layer [32, 36]. As shown in Table 4,  $n_f$  was small, indicating that the compact of corrosion product on X80 steel in the bulk solution was low. Under TEL of 300  $\mu\text{m}$  and 145  $\mu\text{m}$ ,  $R_f$  and  $n_f$  obviously fluctuated with corrosion time, which showed that the formation and dissolution of corrosion product layer alternately occurred on the surface of X80 steel. Moreover,  $R_f$  increased gradually with immersion time, and  $n_f$  was bigger than 0.5, which indicated that the corrosion product layer under TEL of 70  $\mu\text{m}$  was in a stable formation process and had a certain protective.

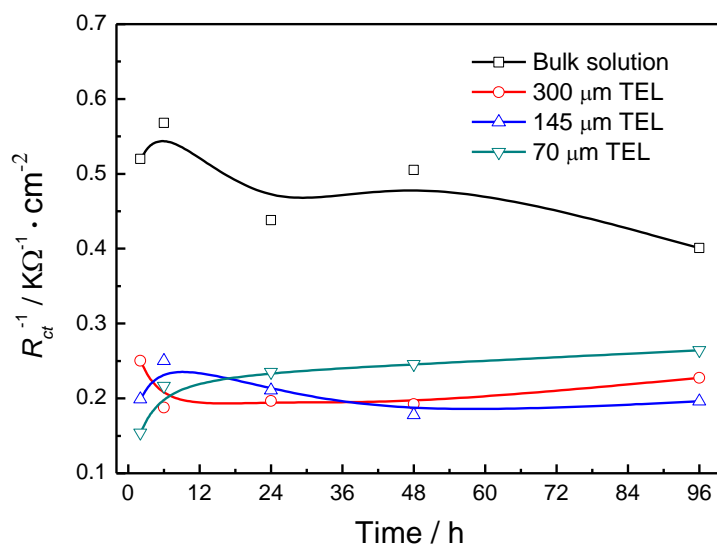


**Figure 6.** Evolution of  $R_{ct}^{-1}$  with immersion time for X80 steel under TEL with various thicknesses

### 3.4 Corrosion morphology

Figure 7 shows the OM and SEM images of X80 steel under TEL with various thicknesses after 96 h exposure. It can be seen that the corrosion products in bulk solution was incomplete and had a small amount of pits (Figure 7a) and obvious holes and micro-cracks (Figure 7b). Besides, the surface morphology of X80 steel after exposure under TEL was significantly different from that in bulk solution, and was dependent on the thickness of TEL.

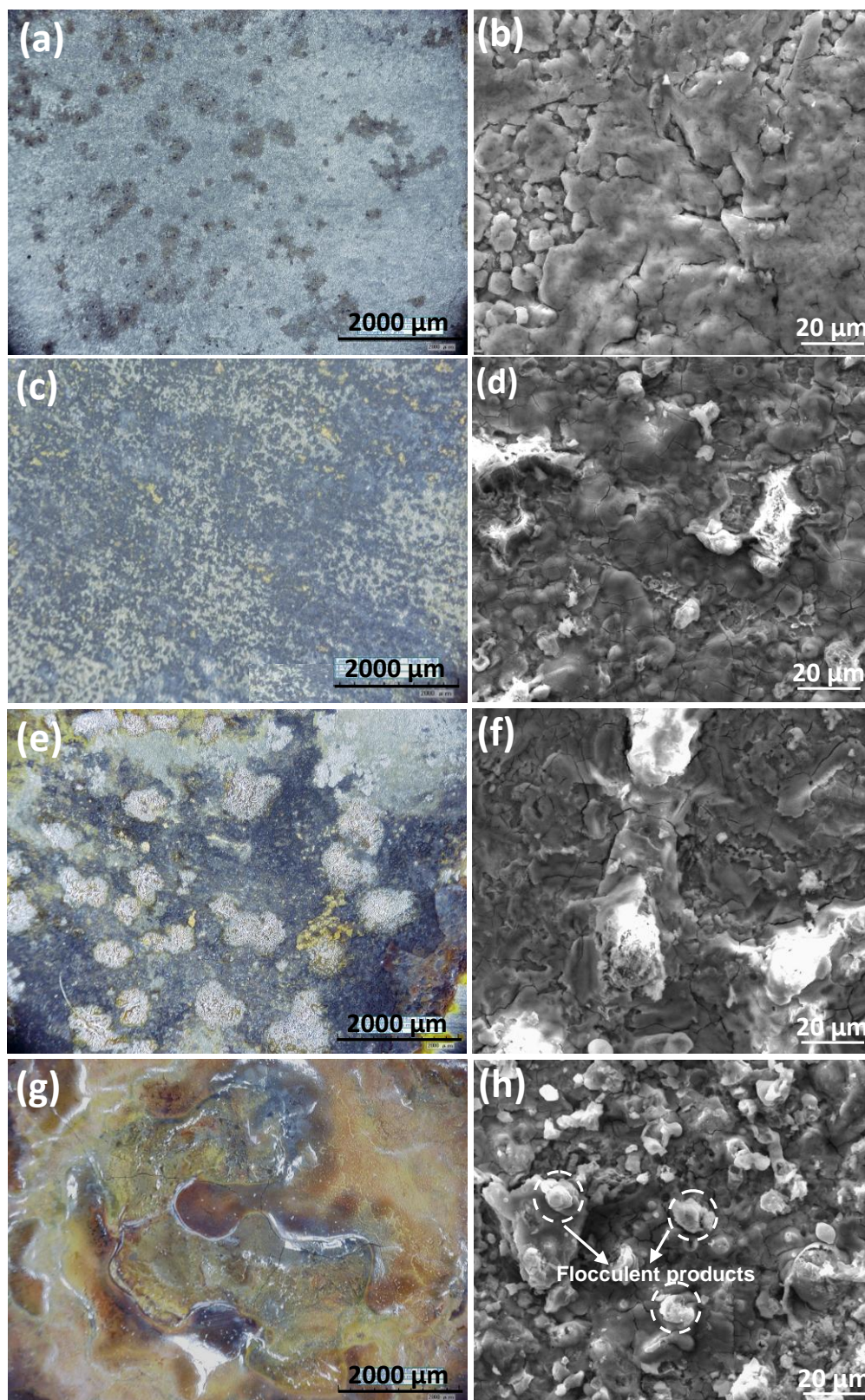


**Figure 7.** OM image (a, c, e, g) and SEM image (b, d, f, h) of X80 steel under TEL with various thicknesses after 96 h exposure. (a, b) bulk solution, (c, d) 300  $\mu\text{m}$  TEL, (e, f) 145  $\mu\text{m}$  TEL, (g, h) 70  $\mu\text{m}$  TEL.

Under TEL of 300  $\mu\text{m}$ , many black corrosion products appeared on X80 steel surface, but was still not completely contiguous (Figure 7c). With the decrease of TEL thickness, the corrosion product layer became more compact but layered. Under TEL of 145  $\mu\text{m}$ , the corrosion products exhibited the distribution of double layers. There were many white snowflake-like corrosion products and few red rust in the external layer, and black corrosion products in the bottomed layer (Figure 7e). Besides, Figure 7f showed that the bottomed corrosion product layer was homogeneous and compact. Under TEL of 70  $\mu\text{m}$ , the corrosion products were still layering. The external corrosion product was mainly yellow rust (Figure 7g). The flocculent particles in the external layer and the uniform corrosion products in the bottomed layer could also be found in Figure 7h, which showed that the corrosion products under 70  $\mu\text{m}$  TEL had good protective effects. Interestingly, the OM and SEM images of X80 steel under different TEL were consistent with the variation laws of  $R_f$  and  $n_f$  fitted by EIS.

### 3.5 Composition of corrosion products

XRD patterns of corrosion product for X80 steel exposed in the TEL with various thicknesses for 96 h are shown in Figure 8. In bulk solution, the phase composition of corrosion product on X80 steel was mainly  $\gamma\text{-FeOOH}$  and  $\text{Fe}_3\text{O}_4$ . The composition and content of corrosion product under TEL were closely related to TEL thickness. Under TEL of 300  $\mu\text{m}$ , the main phase composition of corrosion product was still  $\gamma\text{-FeOOH}$  and  $\text{Fe}_3\text{O}_4$ , but the number and magnitude of the diffraction peaks were obviously less than that in bulk solution. With the decrease of TEL,  $\gamma\text{-FeOOH}$  reduced significantly, and  $\text{Fe}_2\text{O}_3$  had a increasing tendency. Under TEL of 70  $\mu\text{m}$ , the corrosion products were composed of  $\text{Fe}_2\text{O}_3$  and a few  $\gamma\text{-FeOOH}$ . Besides, there was a small amount of  $\text{FeCO}_3$  under TEL of 70  $\mu\text{m}$ . Since  $\text{Fe}_3\text{O}_4$  and  $\text{FeOOH}$  had reducibility [38], so the protective effects of corrosion products in bulk solution and thicker TEL was low.

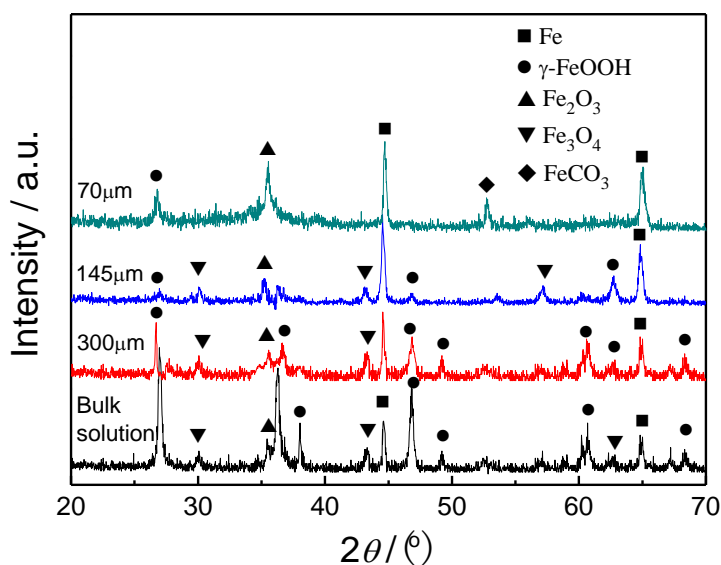


**Figure 8.** XRD pattern of corrosion product for X80 steel under TEL with various thicknesses for 96h

## 4. DISCUSSION

### 4.1 Analysis of corrosion control mechanism

As shown in Figure 4a, double capacitive loops in EIS showed that the corrosion of X80 steel in bulk solution was controlled by the electrochemical activation reaction. Evans diagram (Figure 3) showed that the corrosion of X80 steel was controlled by cathodic process. Oxygen and proton ion ( $H^+$ ) have been recognized as the most common cathodic depolarizers in corrosion process of steel in acidic soils. Although oxygen-consuming corrosion initially occurred, hydrogen evolution corrosion also could happen when oxygen concentration was down to some extent. Therefore, the corrosion of X80 steel in bulk solution was controlled by cathodic electrochemical reaction, including the reduction of  $H^+$  and the ionization reaction of oxygen.

Under TEL, the corrosion control mechanism for X80 steel was closely related to the TEL thickness. Generally, TEL could be divided into the troposphere and the diffusion layer. The oxygen concentration in the troposphere was a constant value, but the oxygen in the diffusion layer had a concentration gradient. The change of TEL thickness mainly affected the thickness of the diffusion layer [27, 29-30]. For the thicker TEL, the thickness of the diffusion layer and the diffusion process of oxygen will not be affected if TEL thickness changes. Assuming that the cathodic process was governed by diffusion of oxygen, the cathodic current density in thicker TEL should not be changed theoretically. The cathodic current density decreased with the decrease of TEL thickness from 300  $\mu m$  to 145  $\mu m$  in Figure 2, which showed that the corrosion of X80 steel in this status was not controlled by diffusion of oxygen. Besides, EIS of X80 steel under TEL of 300  $\mu m$  still displayed the capacitive arcs in Figure 4b, and the corrosion X80 steel under TEL of 300 ~ 200  $\mu m$  was governed by cathodic process (Figure 3). These phenomena together showed that the corrosion of X80 steel was still mainly related to the cathodic electrochemical reaction under TEL of 300  $\mu m$ .

When TEL thickness decreased from 145  $\mu m$  to 100  $\mu m$ , the cathodic current density increased greatly, which showed TEL thickness might be less than the thickness of the diffusion layer in this status. The thinner TEL meant the shorter diffusion path of oxygen. It was generally believed that the corrosion rate of metal was equal to the limit diffusion current of oxygen when the corrosion of metal was controlled by the diffusion of oxygen (Eq. 7) [34]. As shown in Table 3, corrosion current ratio ( $i_{100 \mu m} / i_{145 \mu m} = 1.51$ ) was basically consistent with the inverse ratio of TEL thickness (145  $\mu m / 100 \mu m = 1.45$ ). Besides, Warburg impedance appeared on the low-frequency region of EIS plots for X80 steel under TEL of 145  $\mu m$  (Figure 4c), which fully indicated the diffusion of oxygen dominated the corrosion of X80 steel under TEL of 145  $\mu m$ .

$$i_{\text{corr}} = i_L = nFD_{O_2} \frac{[O_2]}{\delta} \quad (7)$$

Where,  $D_{O_2}$  and  $[O_2]$  are the diffusion coefficient and the concentration of the dissolved oxygen in the electrolyte layer respectively, and  $\delta$  is the diffusion layer thickness,  $n$  is the number of the electrons involved in the oxygen reduction reaction, and  $F$  is the Faraday constant.

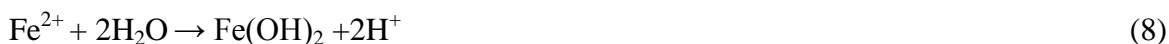
However, the cathodic current density decreased slightly when TEL thickness decreased to 70  $\mu m$  (see Figure 2), which was inconsistent with Eq.7. It indicated that other factors might be involved in the reduction process of oxygen. Researches showed the change of TEL thickness also affected the

diffusion mode of oxygen (one-dimensional or two-dimensional diffusion) [29, 30, 39]. Under TEL of 70  $\mu\text{m}$ , the diffusion of oxygen at the electrode surface might shift from a two-dimensional to one-dimensional. There was more oxygen involved in the reduction process at two-dimensional diffusion, so the cathodic current density under TEL of 70  $\mu\text{m}$  was lower than that of under TEL of 100  $\mu\text{m}$ . Besides, the hydration of metal ions and the diffusion of corrosion product would be greatly affected when TEL thickness changed [30, 37]. In the thinner TEL, the diffusion of corrosion products became more difficult, the extent of anodic polarization increased, the corrosion of X80 steel was jointly controlled by cathodic process and anodic process (Figure 3). In this system, the corrosion rate mainly depends on the diffusion resistance of oxygen and corrosion products, as shown in Warburg impedance in Figure 4d and lower  $Y_w$  in Table 4.

#### 4.2 Discussion of corrosion behavior

The comprehensive results of polarization curves, EIS, OM, SEM and XRD showed that X80 steel in bulk solution and TEL with various thicknesses had different corrosion behavior.

In the bulk solution, the corrosion of X80 steel was controlled by the cathodic electrochemical reaction. Although the depolarization process of oxygen was weak, the reduction process of  $\text{H}^+$  still could be in progress. Besides, the transmission of metal ions and corrosion products in bulk solution was relatively easy, so the anodic process and cathodic process could happen continuously, the corrosion rate was bigger. As corrosion progressed,  $\text{Fe}^{2+}$  generated by anodic reaction could react with the  $\text{OH}^-$  and dissolved oxygen in aqueous phase (Eq.8, 9, 10, 11). An incomplete corrosion product layer,  $\gamma\text{-FeOOH}$  and  $\text{Fe}_3\text{O}_4$ , formed on the surface of X80 steel. The corrosion products could hinder the transmission of metal ion and oxygen, which made the reaction resistance increase, resulting in the decrease of corrosion rate after 24 h exposure. While, the active ions ( $\text{H}^+$ ,  $\text{Cl}^-$ , et al) in simulated solution would dissolve some corrosion product. Micro-holes and micro-cracks would be formed on the corrosion product layer, as shown in Figure 7b. The faults on corrosion product layer provided the channels for the transmission of active ions to the metal substrate, which resulted in the consecutive corrosion.

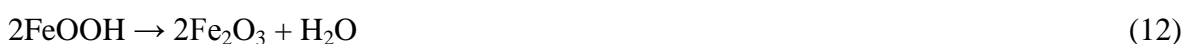


Under TEL of 300  $\mu\text{m}$ , the corrosion of X80 steel was still mainly related to the reduction of  $\text{H}^+$  and the ionization reaction of oxygen. However, compared to the bulk solution, a series of process, including the transmission of oxygen and the accumulation of corrosion product, changed obviously under TEL. Under TEL,  $\text{Fe}^{2+}$  concentration in aqueous phase could easily reach a saturation state [27]. More corrosion product was earlier to form on the electrode, which hindered the diffusion process of oxygen and the metal ions, resulting in the inhibition of corrosion process. It could be explained the phenomenon that the corrosion current density of X80 steel decreased when electrolyte layer thickness decreased from bulk solution to 300  $\mu\text{m}$  (see Figure 2). Whereas, the formation and dissolution of

corrosion product layer occurred alternately on the steel as the corrosion effect of active ions in electrolyte layer, resulting in the fluctuation of corrosion rate for X80 steel under TEL of 300  $\mu\text{m}$ , as shown in Figure 6.

Under TEL of 145  $\mu\text{m}$ , the diffusion of oxygen dominated the corrosion process of X80 steel. In this status, the diffusion path of oxygen was relatively short, the oxygen reached to electrode surface increased, and so the cathodic process of corrosion could be carried out smoothly, resulting in a rapid increase of corrosion rate in 6h. As corrosion progressed, the corrosion products could not be effectively diffused and covered on the electrode surface, a compact and bilayer corrosion product layer was gradually formed (Figure 7c, 7d), which inhibited the anodic process. Besides, the corrosion product layer increased the diffusion resistance of oxygen, the cathodic process weakened. The combined effects resulted in the decrease of corrosion rate in the later stage, as shown in Figure 6.

Under TEL of 70  $\mu\text{m}$ , the shorter diffusion path of oxygen made X80 steel corrode rapidly in the initial stage (6 h). Meanwhile, a complete corrosion product layer was quickly formed as the diffusion of  $\text{Fe}^{2+}$  and corrosion product was greatly inhibited in this status. Corrosion product layer increased the extent of anodic polarization. The corrosion process of X80 steel was gradually controlled by a combination of cathodic process and anodic process, that was, the diffusion of oxygen and corrosion products. However, the thinner electrolyte layer simultaneously made the transmission of active ions to be easier. The accumulation of active ions on the local location of electrode surface intensified the unevenness of the surface potential, so that local corrosion could occur continuously. Therefore, corrosion rate ( $R_{\text{ct}}^{-1}$ ) of X80 steel under 70  $\mu\text{m}$  TEL increased continuously, but increased slowly in the later stage, as shown in Figure 6. Besides,  $\text{Fe}^{2+}$  might react with  $\text{HCO}_3^-$  in electrolyte and formed  $\text{FeCO}_3$  (Eq.13) as the decrease of depolarization effect of oxygen in the later stage. Moreover,  $\text{Fe}_2\text{O}_3$  became the main corrosion product in this status, as shown in Figure 8. Generally,  $\text{Fe}_2\text{O}_3$  was more stable, the protective effect of  $\text{FeCO}_3$  was better than that of  $\text{FeOOH}$  [38], and the bilayer corrosion product layer in this status was more compact, so X80 steel could be passivated, as shown in Figure 2.



## 5. CONCLUSION

(1) In the acidic soil simulated solution, the corrosion of X80 steel was controlled by the charge-transfer process. Under TEL, the corrosion mechanism of X80 steel was dependent on TEL thickness. Under TEL of 300  $\mu\text{m}$ , the corrosion process was still related to the cathodic electrochemical reaction. As TEL reduced to 145  $\mu\text{m}$ , the diffusion process of oxygen dominated the corrosion process of X80 steel. Whereas, the corrosion process of X80 steel was jointly controlled by cathodic process and anodic process under TEL of 70  $\mu\text{m}$ , including the diffusion process of oxygen and corrosion products.

(2) TEL thickness changed, both the diffusion of oxygen and the transmission of corrosion products were influenced. In the bulk solution, X80 steel had higher corrosion rate. Under TEL of 300

$\mu\text{m}$  and  $145\ \mu\text{m}$ , the corrosion rate of X80 steel fluctuated with immersion time. Under TEL of  $70\ \mu\text{m}$ , the corrosion rate increased continuously but increased slowly in the later stage. After 96 h exposure, the corrosion extent of X80 steel with the TEL thickness was in the sequence of  $70\ \mu\text{m} > 300\ \mu\text{m} > 145\ \mu\text{m}$ .

(3) In the bulk solution, an incomplete corrosion product layer,  $\gamma\text{-FeOOH}$  and  $\text{Fe}_3\text{O}_4$ , was formed on the surface of X80 steel. With the decrease of TEL thickness, the corrosion product layer became more compact but layered,  $\gamma\text{-FeOOH}$  reduced significantly. Under TEL of  $70\ \mu\text{m}$ , the bilayer corrosion products, a few of  $\text{Fe}_2\text{O}_3$ ,  $\gamma\text{-FeOOH}$  and  $\text{FeCO}_3$ , was formed.

#### ACKNOWLEDGEMENTS

The authors are grateful to the National Natural Science Foundation of China (No. 51161021) for support to this work.

#### References

1. A. V. Borovikov, *Metallurgist*, 47 (2003) 415-418.
2. J. Niu, L. H. Qi, Y. L. Liu, L. Ma, Y. R. Feng, J. X. Zhang, *Trans. Nonferrous. Met. Soc. China*, 19 (2009) 573-578.
3. A. C. Toncre, *Mater. Performance*, 23 (1984) 22-27.
4. F. Gan, Z. W. Sun, G. Sabde, D. T. Sabde, *Corrosion*, 50 (1994) 804-816.
5. A. Eslami, B. Fang, R. Kania, B. Worthingham, J. Been, R. Eadie, W. Chen, *Corros. Sci.*, 52 (2010) 3750-3756.
6. Z. Wang, J. Wang, E.H. Han, W. Ke, M. Yan, J. Zhang, C. Liu, *Acta Metall. Sin.*, 48 (2012) 1267-1272.
7. E.S. Meresht, T.S. Farahani, J. Neshati, *Eng. Fail. Anal.*, 18 (2011) 963-970.
8. B. Zhao, C. Du, X. Li, Z. Liu, X. Chen, Y. Li, *Sci. Technol. Rev.*, 31 (2013) 72-79.
9. M. C. Yan, J. Q. Wang, E. H. Han, W. Ke, *Corros. Eng. Sci. Technol.*, 42 (2007) 42-49.
10. M. C. Yan, J. Q. Wang, E. H. Han, W. Ke, *Corros. Sci.*, 50 (2008) 1331-1339.
11. F. M. Song, D. W. Kirk, J. W. Graydon, *Mater. Performance*, 42 (2003) 24-26.
12. S. Papavinasam, R. W. Revie, *Corros. Rev.*, 26 (2008) 295-371.
13. A. Eslami, R. Kania, B. Worthingham, G.V. Boven, R. Eadie, W. Chen, *Corrosion*, 69 (2013) 1103-1110.
14. R. Xu, A. Zhao, Q. Li, X. Kong and G. Ji, *Geoderma*, 115 (2003) 75-84.
15. M. C. Yan, C. Sun, J. Xu, J. H. Dong, W. Ke, *Corros. Sci.*, 80 (2014) 309-317.
16. Y.H. Wu, T.M. Liu, C. Sun, J. Xu, C.K. Yu, *Corros. Eng. Sci. Technol.*, 45 (2010) 136-141.
17. K. Mori, K. Tachi, M. Muramats, K. Torita, *Pro. Org. Coat.*, 36 (1999) 34-38.
18. S. A. Arun, L. Uziel, H. P. Joe, *J. Electrochem. Soc.*, 157 (2010) C9-C17.
19. A. Q. Fu, Y. F. Cheng, *Corros. Sci.*, 51 (2009), 914-920.
20. C.F. Dong, A.Q. Fu, X.G. Li, Y.F. Cheng, *Electrochim. Acta*, 54 (2008), 628-633.
21. X. Chen, C. W. Du, X. G. Li, P. Liang, L. Lu, *Int. J. Miner. Metall. Mater.*, 103 (2007) 9-13.
22. J.J. Perdomo, I. Song, *Corros. Sci.*, 42 (2000) 1389-1415.
23. J.J. Perdomo, M.E. Chabica, I. Song, *Corros. Sci.*, 43 (2001) 515-532.
24. Y.Q. Song, C.W. Du, X.G. Li, *J. Univ. Sci. Technol. Beijing*, 13 (2006), 37-43.
25. Y.-S. Choi, J.-G. Kim, *Mater. Sci. Technol.*, 19 (2003) 1737-1745.
26. I. Matsushima, *Corros. Eng.*, 51 (2002) 621-629.
27. A. Q. Fu, X. Tang X, Y. F. Cheng, *Corros. Sci.*, 51 (2009) 186-190.

28. M. C. Yan, J. Q. Wang, E. H. Han, C. Sun, W. Ke, *Acta Metall. Sin.*, 50 (2014) 1137-1145.
29. M. Stratmann, H. Streckel, *Corros. Sci.*, 30 (1990) 681-696.
30. Y. L. Cheng, Z. Zhang, F. H. Cao, J. F. Li, J. Q. Zhang, J. M. Wang, C. N. Cao, *Corros. Sci.*, 46 (2004) 1649-1667.
31. T. Zhang, C. Chen, Y. Shao, G. Meng, F. Wang, X. Li, C. Dong, *Electrochim. Acta*, 53 (2008) 7921-7931.
32. S. X. Wang, D. X. Liu, N. Du, Q. Zhao, S. Y. Li, J. H. Xiao, *Int. J. Electrochem. Sci.*, 10 (2015) 4393-4404.
33. Z. Liu, X. Li, Y. Zhang, C. Du, *Acta Metall. Sin. (Engl. Lett.)*, 22 (2009) 58-64.
34. C. N. Cao, *Principles of Electrochemistry of Corrosion, Third Edition*, Chemical Industry Press, Beijing, 2008 (in Chinese).
35. M. C. Yan, C. Sun, J. Xu, W. Ke, *Int. J. Electrochem. Sci.*, 10 (2015) 1762-1776.
36. L. Hamadou L, A. Kadri, N. Benbrahim, *Appl. Surf. Sci.*, 252 (2005) 1510-1519.
37. X. N. Liao, F. H. Cao, A. N. Chen, W. J. Liu, J. Q. Zhang, C. N. Cao, *Trans. Nonferrous Met. Soc. China*, 22 (2012) 1239-1249.
38. X. H. Nie, X. G. Li, C. W. Du, Y. Z. Huang, H. Du, *J. Raman Spectrosc.*, 40 (2009) 76-79.
39. M. Stratmann, H. Streckel, *Corros. Sci.*, 30 (1990) 697-714.

© 2016 The Authors. Published by ESG ([www.electrochemsci.org](http://www.electrochemsci.org)). This article is an open access article distributed under the terms and conditions of the Creative Commons Attribution license (<http://creativecommons.org/licenses/by/4.0/>).